



# Enhanced high-rate performance of ball-milled $\text{MmNi}_{3.55}\text{Co}_{0.75}\text{Mn}_{0.4}\text{Al}_{0.3}$ hydrogen storage alloys with graphene nanoplatelets



R.C. Cui<sup>a</sup>, C.C. Yang<sup>a,\*</sup>, M.M. Li<sup>a</sup>, B. Jin<sup>a</sup>, X.D. Ding<sup>b,\*\*</sup>, Q. Jiang<sup>a</sup>

<sup>a</sup> Key Laboratory of Automobile Materials, Ministry of Education and School of Materials Science and Engineering, Jilin University, Changchun, 130022, China

<sup>b</sup> State Key Laboratory for Mechanical Behavior of Materials, Xi'an Jiaotong University, Xi'an, 710049, China

## ARTICLE INFO

### Article history:

Received 11 August 2016

Accepted 15 September 2016

Available online 16 September 2016

### Keywords:

Hydrogen storage alloy

High-energy ball milling

Graphene nanoplatelets

High-rate dischargeability

## ABSTRACT

The poor high-rate dischargeability (HRD) of negative electrode materials (hydrogen storage alloys) has impeded applications of nickel metal hydride batteries in high-power fields, electric vehicles, hydride electric vehicles, power tools, modern military devices, etc. Here we report a facile and effective strategy to enhance the HRD performance of commercial  $\text{MmNi}_{3.55}\text{Co}_{0.75}\text{Mn}_{0.4}\text{Al}_{0.3}$  hydrogen storage alloy (here Mm denotes mischmetals) with high-energy ball milling and addition of graphene nanoplatelets (GNPs). At a discharge current density of  $3000 \text{ mA g}^{-1}$ , the capacity retention rate of the alloy electrode could reach 53.0% after ball-milling, and 68.3% after further addition of GNPs, which is 3.2 times that of original alloy electrode (21.5%). Such a superior HRD performance is contributed by (1) smaller particle size of alloys to reduce the diffusion distance of hydrogen atoms; (2) high conductivity of GNPs to accelerate the charge transfer; and (3) interconnected GNPs among alloys to decrease the internal resistance.

© 2016 Elsevier B.V. All rights reserved.

## 1. Introduction

The rechargeable nickel-metal hydride (Ni-MH) batteries have been widely used in portable electronics, power tools, electric vehicles, hydride electric vehicles, military devices, etc., owing to their high safety, excellent performance at low/high temperatures, and superior environmental friendliness [1,2]. The traditional AB<sub>5</sub>-type hydrogen storage alloy,  $\text{MmNi}_{3.55}\text{Co}_{0.75}\text{Mn}_{0.4}\text{Al}_{0.3}$ , is commercially used in Ni-MH battery as its negative electrode material, where Mm denotes mischmetals here and this alloy is called as c-AB<sub>5</sub> later [3]. It is desirable to enhance the high-rate dischargeability (HRD) property of hydrogen storage alloys, which dominates applications of Ni-MH battery in high-power fields [4,5]. Thus, numerous efforts have been implemented to focus on this topic in recent years, such as composition optimization [6,7], additives [8,9], surface modifications [10], composites formation [11], etc. These methods are effective and have enhanced the HRD

performance of hydrogen storage alloys. However, the development of novel electrode materials for applications in high-power Ni-MH batteries is still on the way.

It has been demonstrated that the HRD performance of Ni-MH electrode is determined by the diffusion rate of hydrogen atoms in hydrogen storage alloys and the electrochemical reaction rate on the electrode surface [12–14]. On the basis of this principle, the HRD property of Ni-MH electrode could be enhanced by (i) reducing the particle size of hydrogen storage alloys to decrease the diffusion distance of hydrogen atoms; and (ii) decreasing the contact resistance  $R_c$  and charge-transfer resistance  $R_{ct}$  to accelerate the electrochemical reaction on the electrode surface. Ball-milling is an effective and widely-adopted method to decrease the particle size and to form structural defects through the cycling cut and deformation [15]. Moreover, high-conductivity additives, such as carbon black, carbon nanotubes (CNTs) and carbon nanospheres (CNE), could effectively decrease  $R_c$  and  $R_{ct}$  [16–18]. Graphene, an amazing two-dimensional material [single-layer or few layers (<10)] with large surface area, has exhibited superior electrical conductivity, chemical stability and structural flexibility [19,20], which enable it to be an excellent additive in energy storage devices to improve their HRD properties [21]. Recently, graphene/hydrogen storage alloys composites have been fabricated, showing superior

\* Corresponding author.

\*\* Corresponding author.

E-mail addresses: [ccyang@jlu.edu.cn](mailto:ccyang@jlu.edu.cn) (C.C. Yang), [dingxd@mail.xjtu.edu.cn](mailto:dingxd@mail.xjtu.edu.cn) (X.D. Ding).

HRD performance [12,22]. This is because graphene could act as bridges to connect active particles and significantly decrease the internal resistance and polarization of hydrogen storage alloys.

In this work, a combination of ball-milling and graphene nanoplatelets (GNPs) addition was used to improve the HRD performance of c-AB<sub>5</sub> alloy. The fabricated hybrid electrode shows a capacity retention rate of 68.3% at a discharge current density of 3000 mA g<sup>-1</sup>, which is 3.2 times that of bare alloy electrode. The effects of ball-milling and GNPs are investigated individually. The facile and effective strategy proposed in this paper provides a new approach to enhance the HRD performance of hydrogen storage alloys.

## 2. Experimental

The as-cast c-AB<sub>5</sub> alloy was prepared by radio-frequency inductive melting method, which was described in detail elsewhere [12]. In order to individually investigate the effects of ball-milling and GNPs addition on HRD properties of the above alloy, we prepared three samples with different processes. The sample 1 (S1) is as-melted c-AB<sub>5</sub> alloy powders with an average particle diameter of 50 ± 10 μm. The sample 2 (S2) is ball-milled S1 for 30 min by using SPEX 8000 Mixer/Mill. S1 was placed in a stainless steel jar with a ball-to-powder weight ratio of 10:1 and the jar was sealed in a glove box at an atmosphere of argon followed by ball-milling for 30 min. The sample 3 (S3) is ball-milled S1 with GNPs (Aladdin, the purity > 99.5%) for 30 min. The ball-milling procedure is the same as S2.

The phase structures were examined by X-ray diffraction (XRD, D/max2500pc diffractometer, Cu-K<sub>α</sub> radiation) measurements. Raman spectrum was performed by a micro-Raman spectrometer (Renishaw) with a laser of 532-nm excitation wavelength. The morphologies of the three samples were characterized with a field-emission scanning electron microscope (FESEM, JSM-6700F, JEOL, 15 keV) and a transmission electron microscope (TEM, JEM-2100F, JEOL, 200 keV). The details of electrodes (S1, S2 and S3) preparation and electrochemical measurements are given elsewhere [12]. The HRD performance is characterized by:

$$HRD = C_d / C_{max} \times 100\% \quad (1)$$

where  $C_d$  denotes the discharge capacities of electrodes measured at different discharge current densities  $I_c$  ( $I_c = 300, 600, 900, 1200, 1500, 2400, 3000$  mA g<sup>-1</sup>, respectively), and  $C_{max}$  is the maximum discharge capacity at  $I_c = 60$  mA g<sup>-1</sup> after 4-cycle activation. The electrochemical impedance spectra (EIS), linear polarization curves

and anode polarization curves were tested using an IVIUM electrochemical analyzer according to procedures described in detail elsewhere [12].

## 3. Results and discussions

Fig. 1a shows XRD patterns of S1, S2 and S3, which retain typical CaCu<sub>5</sub>-type hexagonal structure with a space group of P6/mmm [12,23]. This indicates that (1) the ball-milling produces no new phases; and (2) a tiny amount of GNPs (1.15 wt% as measured by an inductively coupled plasma analyzer) in S3 have limited effect on the diffraction reflections of the composite. Obviously, the diffraction peaks become broader from S1 to S2 and S3, implying smaller grain sizes of S2 and S3 than that of S1 after ball-milling treatment and lots of defects generated during ball milling [10,22]. Fig. 1b compares Raman spectra of S3 and pristine GNPs. The spectrum of the latter exhibits a weak D band (1352 cm<sup>-1</sup>) and a prominent G band (1580 cm<sup>-1</sup>), which correspond to the defects (and disorders) and the E<sub>2g</sub> vibration of sp<sup>2</sup> carbon atoms in GNPs, respectively [24]. Compared with pristine GNPs, the D band of S3 is broadened and the intensity ratio of the D band to G band ( $I_d/I_g$ ) increases from 0.17 to 0.74, indicating increases of defects and disorders, and a decrease in the average size of sp<sup>2</sup> domains in S3 from the mechanical shear exfoliation of GNPs during the ball-milling process [12,24].

Fig. 2a–c represent SEM images of S1, S2 and S3, respectively. As noted above, the average particle diameter of S1 is 50 ± 10 μm. After 30-min ball milling, the particle size decreases to 1–12 μm for S2 (Fig. 2b) and 1–8 μm for S3 (Fig. 2c), respectively. These results are consistent with the analysis of XRD mentioned above. The GNPs in S3 could act as process control agent during the ball-milling process, which reduces the effect of cold welding and inhibits agglomeration [25], resulting in smaller particle size and more homogeneous size distribution of S3 than those of S2. Moreover, it is clear from Fig. 2a that the surface of S1 is smooth with clear edges and corners of the particles. On the contrary, the edges and corners of the alloy particles become indistinct and the surface becomes rough in S2 and S3, which generate more reactive surface and active sites. Fig. 2d exhibits a high-magnification SEM image of S3, where the GNPs could perform as bridges to connect active particles (see the dashed circle in the figure), decreasing the internal resistance and polarization of the c-AB<sub>5</sub> alloy significantly [22]. The morphology of the GNPs in S3 is further characterized through TEM, as displayed in Fig. 2e and f. It is evident that the GNPs are closely connected with each other, maintaining two-dimensional sheet-like structures, which provide high conductivity [26].

Fig. 3a plots the discharge capacity curves of S1, S2 and S3

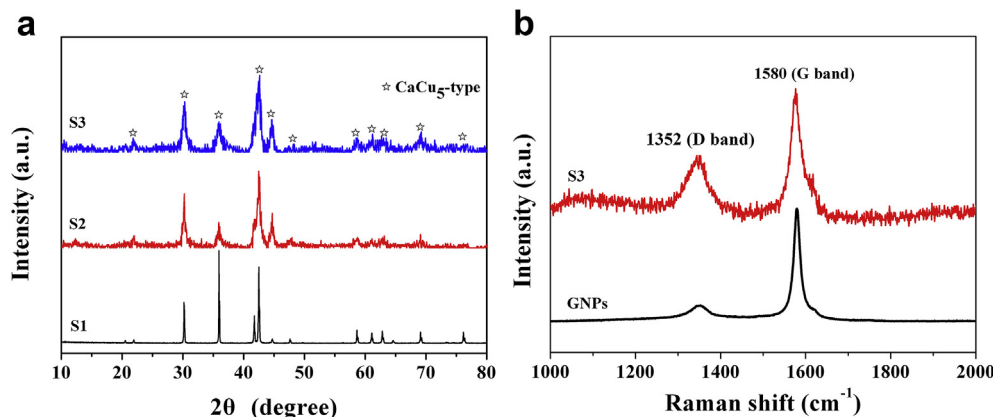
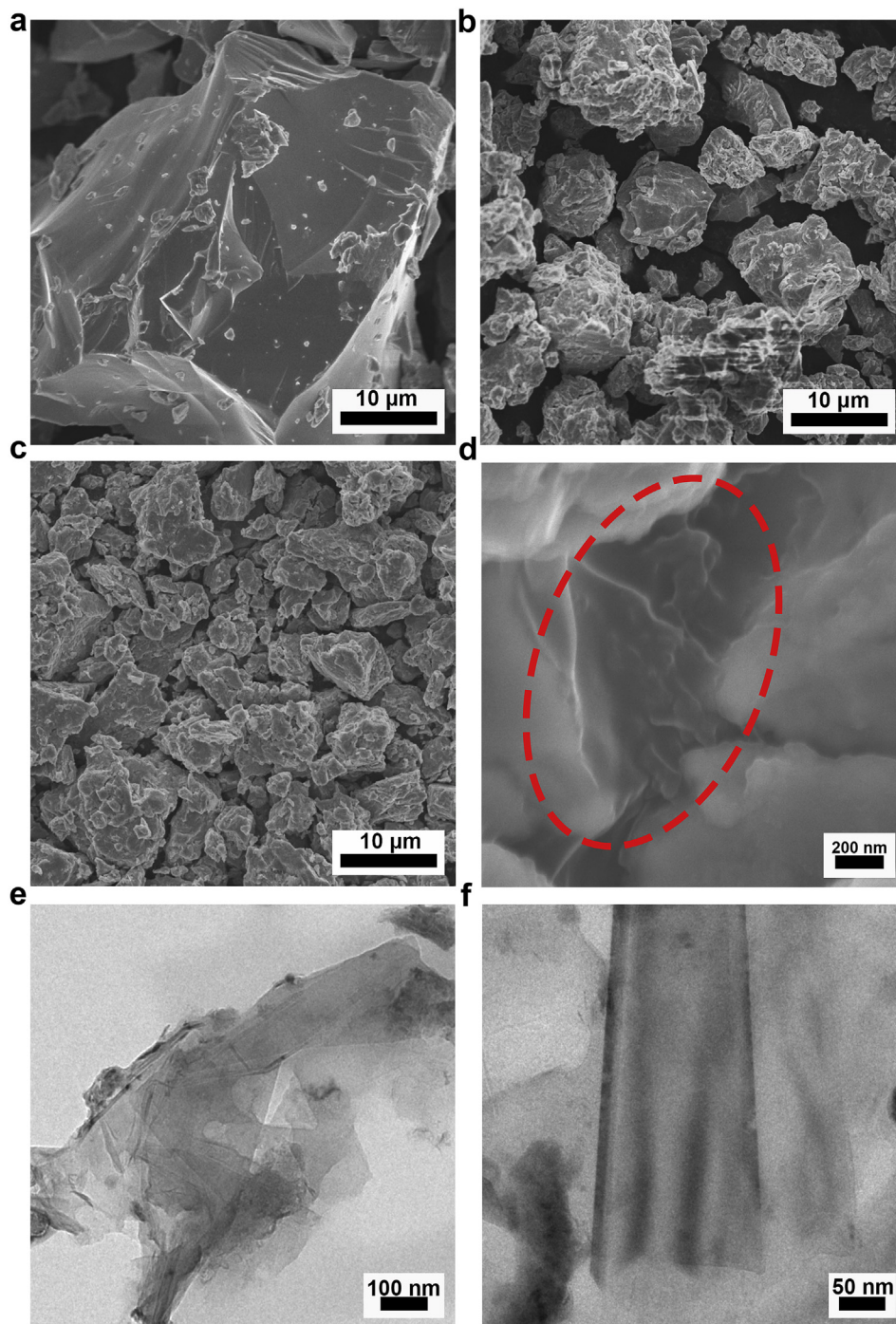


Fig. 1. XRD patterns and Raman spectra. (a) XRD patterns of S1, S2 and S3. (b) Raman spectra of pristine GNPs and S3.



**Fig. 2.** Morphological characterizations of S1, S2 and S3. (a)–(c) are SEM images of S1, S2 and S3, respectively. (d) The high-magnification SEM image of S3. (e)–(f) are low- and high-magnification TEM images of GNPs in S3.

electrodes. The corresponding  $C_{\max}$  values listed in Table 1 are 319.4, 234.2 and 258.9  $\text{mAh g}^{-1}$ , respectively. The smaller  $C_{\max}$  values of S2 and S3 than that of S1 are related to their partial amorphization after ball milling [10]. As for slightly larger  $C_{\max}$  value of S3 than that of S2, the GNPs could adsorb hydrogen in electrochemical reaction [27,28]. Compared with S1, S2 and S3 show excellent activation characteristics (see Fig. 3b). They could reach their  $C_{\max}$  values without activation process, while S1 required 4 cycles for its full activation. This is caused by their increasing specific surface areas and more diffusion channels

(structure defects) for proton ( $\text{H}^+$ ) generated by the ball-milling treatment [15,29,30]. Fig. 3c illustrates HRD performance of the three electrodes at different  $I_c$ . It is found that the HRD property of S3 is better than those of S1 and S2 at almost all  $I_c$  values and the difference between them becomes larger with increasing  $I_c$ . From Table 1, the capacity retention rates are 21.5%, 53.0% and 68.3% for S1, S2 and S3, respectively, at  $I_c = 3000 \text{ mA g}^{-1}$  (10C). Obviously, S3 shows the best HRD performance and its capacity retention rate is 3.2 times that of S1. Correspondingly, the discharge capacities  $C_{3000}$  of S1, S2 and S3 electrodes at  $I_c = 3000 \text{ mA g}^{-1}$  are 68.7, 124.1 and

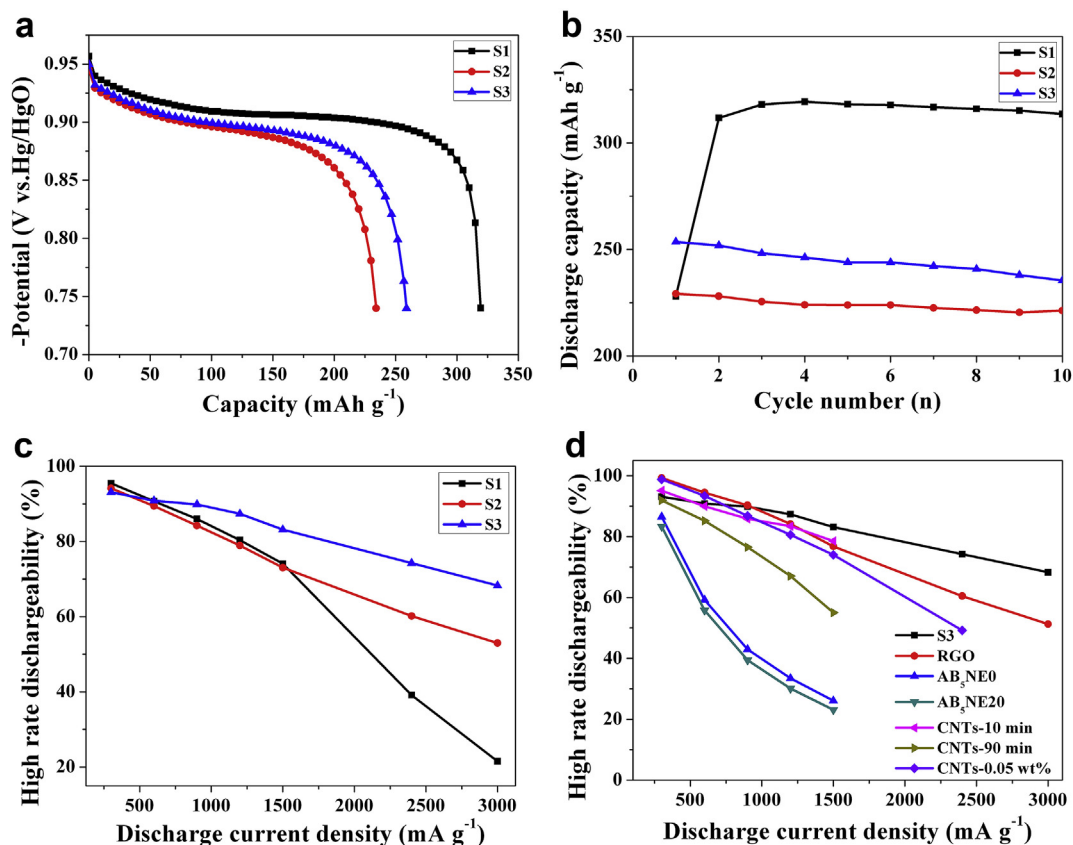


**Fig. 3.** Discharge capacities and HRD properties. (a) The discharge capacities of S1, S2 and S3. (b) Activation of S1, S2 and S3. (c) The HRD properties of S1, S2 and S3. (d) Comparisons of HRD properties of S3 and AB<sub>5</sub>-type hydrogen storage alloys reported in open literature from other methods, including the incorporation of RGO [12] or CNTs (CNTs-0.05 wt%) [17], other ball milling with different additions, such as CNE and different proportions of Ni (0 and 20%) (AB<sub>5</sub>NE0 and AB<sub>5</sub>NE20) [18], ball milling with CNTs for different time (CNTs-10 min and CNTs-90 min) [31].

**Table 1**  
Electrochemical properties of S1, S2 and S3 electrodes.

Samples	$C_{\max}$ (mAh g <sup>-1</sup> )	$C_{3000}$ (mAh g <sup>-1</sup> )	HRD <sub>3000</sub> (%)	$R_c$ (mΩ)	$R_{ct}$ (mΩ)	$I_0$ (mA g <sup>-1</sup> )	$I_L$ (mA g <sup>-1</sup> )
S1	319.4	68.7	21.5	240	290	105.1	3224.2
S2	234.2	124.1	53.0	187	235	118.9	3296.8
S3	258.9	176.8	68.3	136	155	161.6	4643.6

176.8 mAh g<sup>-1</sup>, respectively (see Table 1). S3 owns the largest  $C_{3000}$  although its  $C_{\max}$  value is smaller than that of S1. Recently, we ever reported the design and synthesis of a composite of reduced graphite oxide (RGO)/hydrogen storage alloys via a facile top-down

route [12]. The composite electrode shows an enhanced HRD performance with a capacity retention rate of 51.25% at  $I_c = 3000$  mA g<sup>-1</sup>. The combination of ball-milling and addition of GNPs proposed in this work shows more enhanced HRD

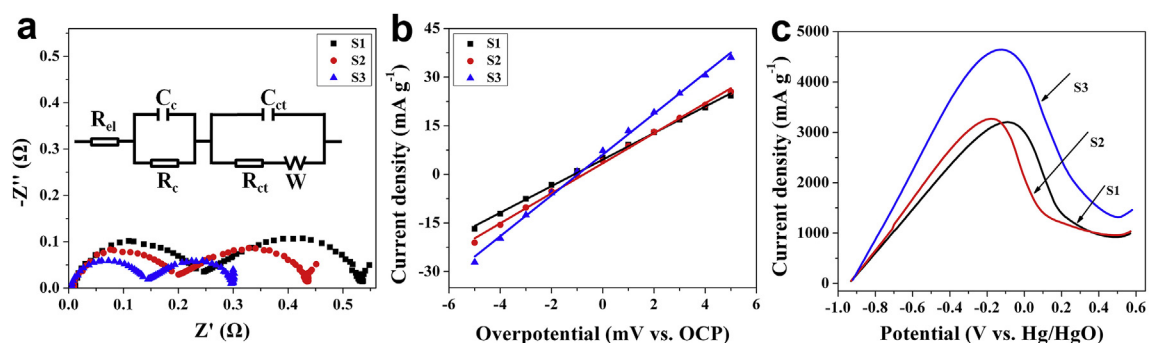


**Fig. 4.** Electrochemical measurements results of S1, S2 and S3 electrodes at room temperature. (a) Electrochemical impedance spectra at 50% DOD. (b) Linear polarization curves at 50% DOD (here OCP means the open circuit potential). (c) Anodic polarization curves at 50% DOD.

performance of AB<sub>5</sub>-type hydrogen storage alloys. Moreover, for comparisons, Fig. 3d shows HRD properties of S3 and AB<sub>5</sub>-type hydrogen storage alloys reported in open literature from other methods, such as the incorporation of RGO [12] or CNTs [17], other ball milling with different additions (CNE and CNTs) [18,31]. It is clear that the HRD performance of S3 is the best at larger  $I_c$  ( $I_c > 900 \text{ mA g}^{-1}$ ) among these results.

In order to explore mechanisms behind the enhanced HRD property of S3, we take a series of electrochemical measurements of the three electrodes: EIS, linear polarization curves and anodic polarization curves at 50% depth of discharge (DOD) [12]. Fig. 4a represents the EIS measurement results, where each spectrum is composed of three regions, a smaller semicircle at the high-frequency region, a larger semicircle and a straight line in the low-frequency zone. The smaller semicircle is related to  $R_c$  among alloy particles, or between the current collector and alloy powders. The larger semicircle reflects  $R_{ct}$  of the electrode, while the straight line denotes the Warburg impedance relating to the diffusion of hydrogen from the alloy surface to interior [12,32]. The smaller the semicircle is, the smaller the resistance is. As shown in Fig. 4a, both radii decrease from S1 to S3, which indicates that  $R_c$  and  $R_{ct}$  become smaller correspondingly. This can be verified by their  $R_c$  and  $R_{ct}$  values as listed in Table 1, which are obtained according to the equivalent circle (the inset in Fig. 4a) [12]. It is evident that S3 owns the smallest  $R_c$  and  $R_{ct}$ , depressing the polarization significantly. Fig. 4b displays linear polarization curves of S1, S2 and S3. When the variation of the overpotential is smaller than 10 mV, the exchange current density ( $I_0$ ), which reflects the rate of electrochemical reaction at the electrode/electrolyte interface, is given by:

$$I_0 = RTI_d/F\eta \quad (2)$$

where  $R$  is the ideal gas constant,  $T$  the absolute temperature,  $I_d$  the applied current density,  $F$  the Faraday constant, and  $\eta$  the whole overpotential [23]. Based on the slope of linear polarization curves,  $I_0$  values of S1, S2 and S3 are obtained and also listed in Table 1. The  $I_0$  value of S3 ( $161.6 \text{ mA g}^{-1}$ ) is larger than those of S2 ( $118.9 \text{ mA g}^{-1}$ ) and S1 ( $105.1 \text{ mA g}^{-1}$ ), implying the best hydrogen absorption and desorption kinetics of S3. Fig. 4c plots anodic polarization curves of S1, S2 and S3. The current density increases with increasing overpotential and reaches a maximum value, which is defined as the limiting current density ( $I_L$ ) [12,33].  $I_L$  reflects the diffusion rate of hydrogen atoms from the bulk to surface of alloy electrodes, and the larger the  $I_L$  value, the faster the hydrogen diffusion. From Fig. 4c, the  $I_L$  values are 3224.15, 3296.83 and 4643.60  $\text{mA g}^{-1}$  for S1, S2 and S3, respectively. Summarizing the above finding, both the fastest electrochemical reaction rate on the electrode surface and hydrogen diffusion rate within alloys contribute to the best HRD performance of S3 due to the effects of ball-milling and excellent conductivity of GNPs.

#### 4. Conclusions

In summary, an effective tactic was reported to improve the HRD performance of c-AB<sub>5</sub> alloy by ball-milling and GNPs addition, which bring small particle size, high conductivity, and interconnected GNPs among alloys. Thus, S3 owns the smallest  $R_c$  and  $R_{ct}$  and the largest  $I_0$  and  $I_L$ , indicating the faster electrochemical reaction rate on the electrode surface and hydrogen diffusion rate within alloys, which lead to excellent initial activation and superior HRD performances. At a discharge current density of  $3000 \text{ mA g}^{-1}$ , the capacity retention rate of S3 could reach 68.3%, which is 3.2 times that of S1. S3 is a promising candidate for applications in high-power Ni-MH batteries and the simple and facile method reported in this work can also be extended to other hydrogen

storage alloy systems.

#### Acknowledgements

We wish to thank ChangBai Mountain Scholars Program, Natural Science Foundation of Jilin Province (No. 20160101315JC), Open Project of State Key Laboratory for Mechanical Behavior of Materials (20151707), Special Fund for Industrial Innovation in Jilin Province (No. 2016C039), and Graduate Innovation Fund of Jilin University (No. 2016169) for financially supporting this project.

#### References

- [1] S.R. Ovshinsky, M.A. Fetcenko, J. Ross, A nickel metal hydride battery for electric vehicles, *Science* 260 (1993) 176–181.
- [2] L. Schlapbach, A. Züttel, Hydrogen-storage materials for mobile applications, *Nature* 414 (2001) 353–358.
- [3] S. Srivastava, R.K. Upadhyay, Investigations of AB<sub>5</sub>-type negative electrode for nickel-metal hydride cell with regard to electrochemical and microstructural characteristics, *J. Power Sour.* 195 (2010) 2996–3001.
- [4] P. Taheri, M. Yazdanpour, M. Bahrami, Analytical assessment of the thermal behavior of nickel-metal hydride batteries during fast charging, *J. Power Sour.* 245 (2014) 712–720.
- [5] F. Li, K. Young, T. Ouchi, M.A. Fetcenko, Annealing effects on structural and electrochemical properties of (LaPrNdZr)<sub>0.83</sub>Mg<sub>0.17</sub>(NiCoAlMn)<sub>3.3</sub> alloy, *J. Alloys Compd.* 471 (2009) 371–377.
- [6] Y. Fukumoto, M. Miyamoto, M. Matsuoka, C. Iwakura, Effect of the stoichiometric ratio on electrochemical properties of hydrogen storage alloys for nickel-metal hydride batteries, *Electrochim. Acta* 40 (1995) 845–848.
- [7] H.G. Pan, S. Ma, J. Shen, J.J. Tan, J.L. Deng, M.X. Gao, Effect of the substitution of Pr for La on the microstructure and electrochemical properties of La<sub>0.7-x</sub>Pr<sub>x</sub>Mg<sub>0.3</sub>Ni<sub>2.45</sub>Co<sub>0.75</sub>Mn<sub>0.1</sub>Al<sub>0.2</sub> ( $x=0.0-0.3$ ) hydrogen storage electrode alloys, *Int. J. Hydrog. Energ.* 32 (2007) 2949–2956.
- [8] T. Sakai, H. Ishikawa, K. Oguro, Effects of microencapsulation of hydrogen storage alloy on the performances of sealed nickel/metal hydride batteries, *J. Electrochem. Soc.* 134 (1987) 558–562.
- [9] P. Zhang, X.D. Wei, Y.N. Liu, J.W. Zhu, G. Yu, Effects of metal oxides addition on the performance of La<sub>1.3</sub>CaMg<sub>0.7</sub>Ni<sub>9</sub> hydrogen storage alloy, *Int. J. Hydrog. Energ.* 33 (2008) 1304–1309.
- [10] S. Li, G.L. Pan, X.P. Gao, J.Q. Qu, F. Wu, D.Y. Song, The electrochemical properties of MnNi<sub>3.6</sub>Co<sub>0.7</sub>Al<sub>0.3</sub>Mn<sub>0.4</sub> alloy modified with carbon nanomaterials by ball milling, *J. Alloys Compd.* 364 (2004) 250–256.
- [11] H.M. Du, L.F. Jiao, Q.H. Wang, W.X. Peng, D.W. Song, Y.J. Wang, H.T. Yuan, Structure and electrochemical properties of ball-milled Co-carbon nanotube composites as negative electrode material of alkaline rechargeable batteries, *J. Power Sour.* 196 (2011) 5751–5755.
- [12] M.M. Li, C.C. Yang, L.X. Chen, Q. Jiang, Hydrogen storage alloys/reduced graphite oxide: an efficient hybrid electrode with enhanced high-rate dischargeability, *Electrochim. Acta* 200 (2016) 59–65.
- [13] M.M. Li, C.C. Yang, W.T. Jing, B. Jin, X.Y. Lang, Q. Jiang, *In situ* grown Co<sub>3</sub>O<sub>4</sub> on hydrogen storage alloys for enhanced electrochemical performance, *Int. J. Hydrog. Energ.* 41 (2016) 8946–8953.
- [14] M.M. Li, C.C. Yang, C.C. Wang, Z. Wen, Y.F. Zhu, M. Zhao, J.C. Li, W.T. Zheng, J.S. Lian, Q. Jiang, Design of hydrogen storage alloys/nanoporous metals hybrid electrodes for nickel-metal hydride batteries, *Sci. Rep.* 6 (2016) 27601.
- [15] H. Chen, J.M. Wang, T. Pan, H.M. Xiao, J.Q. Zhang, C.N. Cao, Effects of high-energy ball milling (HEBM) on the structure and electrochemical performance of nickel hydroxide, *Int. J. Hydrog. Energ.* 28 (2003) 119–124.
- [16] W.K. Zhang, X.H. Xia, H. Huang, Y.P. Gan, J.B. Wu, J.P. Tu, High-rate discharge properties of nickel hydroxide/carbon composite as positive electrode for Ni/MH batteries, *J. Power Sour.* 184 (2008) 646–651.
- [17] S. Li, G.L. Pan, Y. Zhang, X.P. Gao, J.Q. Qu, J. Yan, F. Wu, D.Y. Song, Electrochemical properties of MnNi<sub>3.6</sub>Co<sub>0.7</sub>Al<sub>0.3</sub>Mn<sub>0.4</sub> alloy containing carbon nanotubes, *J. Alloys Compd.* 353 (2003) 295–300.
- [18] D.J. Cuscuetta, H.L. Corso, A. Arenillas, P.S. Martinez, A.A. Ghilarducci, H.R. Salva, Electrochemical effect of carbon nanospheres on an AB<sub>5</sub> alloy, *Int. J. Hydrog. Energ.* 37 (2012) 14978–14982.
- [19] A.K. Geim, Graphene: status and prospects, *Science* 324 (2009) 1530–1534.
- [20] M.J. Allen, V.C. Tung, R.B. Kaner, Honeycomb carbon: a review of graphene, *Chem. Rev.* 110 (2010) 132–145.
- [21] Z.S. Wu, W.C. Ren, L. Xu, F. Li, H.M. Cheng, Doped graphene sheets as anode materials with superhigh rate and large capacity for lithium ion batteries, *ACS Nano* 5 (2011) 5463–5471.
- [22] L.Z. Ouyang, Z.J. Cao, L.L. Li, H. Wang, J.W. Liu, D. Min, Y.W. Chen, F.M. Xiao, R.H. Tang, M. Zhu, Enhanced high-rate discharge properties of La<sub>1.3</sub>Mg<sub>6.0</sub>Sm<sub>7.4</sub>Ni<sub>61.0</sub>Co<sub>7.2</sub>Al<sub>7.1</sub> with added graphene synthesized by plasma milling, *Int. J. Hydrog. Energ.* 39 (2014) 12765–12772.
- [23] Y.F. Liu, H.G. Pan, M.X. Gao, Q.D. Wang, Advanced hydrogen storage alloys for Ni/MH rechargeable batteries, *J. Mater. Chem.* 21 (2011) 4743–4755.
- [24] J.X. Song, Z.X. Yu, M.L. Gordin, S. Hu, R. Yi, D.H. Tang, T. Walter, M. Regula, D. Choi, X.L. Li, A. Manivannan, D.H. Wang, Chemically bonded Phosphorus/

- Graphene hybrid as a high performance anode for sodium-ion batteries, *Nano Lett.* 14 (2014) 6329–6335.
- [25] C. Suryanarayana, Mechanical alloying and milling, *Prog. Mater. Sci.* 46 (2001) 1–184.
- [26] G. Liu, Y.J. Wang, C.C. Xu, F.Y. Qiu, C.H. An, L. Li, L.F. Jiao, H.T. Yuan, Excellent catalytic effects of highly crumpled graphene nanosheets on hydrogenation/dehydrogenation of magnesium hydride, *Nanoscale* 5 (2013) 1074–1081.
- [27] C. Nützenadel, A. Züttel, D. Chartouni, L. Schlapbach, Electrochemical storage of hydrogen in nanotube materials, *Electrochem. Sol. State Lett.* 2 (1999) 30–32.
- [28] K. Jurewicz, E. Frackowiak, F. Béguin, Enhancement of reversible hydrogen capacity into activated carbon through water electrolysis, *Electrochem. Sol. State Lett.* 4 (2001) A27–A29.
- [29] J.H. Jung, K.Y. Lee, J.Y. Lee, The activation mechanism of Zr-based alloy electrodes, *J. Alloys Compd.* 226 (1995) 166–169.
- [30] M.S. Wu, H.R. Wu, Y.Y. Wang, C.C. Wan, Surface treatment for hydrogen storage alloy of nickel/metal hydride battery, *J. Alloys Compd.* 302 (2000) 248–257.
- [31] L.A. Benavides, D.J. Cuscueta, A.A. Ghilarducci, MWCNT as mechanical support during ball milling of an AB<sub>5</sub> alloy used as negative electrode of a Ni-MH battery, *Int. J. Hydrog. Energ.* 40 (2015) 4925–4930.
- [32] X. Li, T. Yang, Y.H. Zhang, D.L. Zhao, H.P. Ren, Kinetic properties of La<sub>2</sub>Mg<sub>17-x</sub> wt.% Ni ( $x=0-200$ ) hydrogen storage alloys prepared by ball milling, *Int. J. Hydrog. Energ.* 39 (2014) 13557–13563.
- [33] C.S. Wang, M.P. Soriaga, S. Srinivasan, Determination of reaction resistances for metal-hydride electrodes during anodic polarization, *J. Power Sour.* 85 (2000) 212–223.